

# Rapid electronic detection of probe-specific microRNAs using thin nanopore sensors

Meni Wanunu<sup>1\*†</sup>, Tali Dadosh<sup>1†</sup>, Vishva Ray<sup>1</sup>, Jingmin Jin<sup>2</sup>, Larry McReynolds<sup>2</sup> and Marija Drndić<sup>1\*</sup>

**Small RNA molecules have an important role in gene regulation and RNA silencing therapy, but it is challenging to detect these molecules without the use of time-consuming radioactive labelling assays or error-prone amplification methods. Here, we present a platform for the rapid electronic detection of probe-hybridized microRNAs from cellular RNA. In this platform, a target microRNA is first hybridized to a probe. This probe: microRNA duplex is then enriched through binding to the viral protein p19. Finally, the abundance of the duplex is quantified using a nanopore. Reducing the thickness of the membrane containing the nanopore to 6 nm leads to increased signal amplitudes from biomolecules, and reducing the diameter of the nanopore to 3 nm allows the detection and discrimination of small nucleic acids based on differences in their physical dimensions. We demonstrate the potential of this approach by detecting picogram levels of a liver-specific miRNA from rat liver RNA.**

**M**icroRNAs (miRNAs), initially identified in *Caenorhabditis elegans* in 1993 (ref. 1), are small endogenous biomolecules that have an important regulatory role in embryonic differentiation, haematopoiesis, cardiac hypertrophy and a variety of cancers<sup>2,3</sup>. MiRNAs act by associating with the RNA-induced silencing complex, which binds to messenger RNA and inhibits protein synthesis. RNA interference, discovered in 1998 (ref. 4), is a related process in which small RNA is used for silencing genes. The impact of small RNA on gene expression has led to its adoption as both a research reagent and as a potential therapeutic for silencing cancer and disease-related genes<sup>5</sup>. Efforts in biology are now aimed at understanding the function of small RNAs and miRNAs, and at designing and evaluating the efficacy of RNA-derived silencing drugs<sup>6,7</sup>. However, detection of small cellular RNA without error-prone reverse transcriptase–polymerase chain reaction (RT-PCR) amplification<sup>8</sup> remains challenging, as the few copies of miRNA must be distinguished from other more abundant molecules.

Almost four decades after the invention of the Coulter counter, which can sense blood or pathogen cells as they pass through a microchannel between two chambers filled with electrolytic solutions<sup>9</sup>, nanopores have emerged as molecular counters<sup>10–12</sup> with great promise for single-molecule analysis. The need for nanopores of adjustable dimensions has stimulated approaches for engineering protein channels<sup>13,14</sup> and producing physically robust synthetic pores<sup>15</sup>. Advances in nanopore fabrication in silicon nitride (SiN) membranes using ion<sup>16</sup> or electron<sup>17</sup> beams have enabled the detection of nucleic acids, proteins and biomolecular complexes<sup>18–28</sup>, and have also inspired sophisticated approaches for DNA sequencing<sup>29</sup>.

Biomolecule detection using nanopores in synthetic membranes as thin as lipid membranes (5–6 nm) is complicated, presumably because of limited membrane stability. Recently, several groups have independently reported on the use of graphene as a membrane material for nanopore-based biomolecular detection<sup>30–32</sup>. In this work, we show that thinning a submicrometre area of a SiN membrane provides uniform and robust membranes with thicknesses as small as 6 nm. Decreasing the membrane thickness increases the signal amplitudes of biomolecules, while only slightly speeding up DNA transport through the pore. Furthermore, 3-nm-diameter

pores in sub-10-nm membranes facilitate the detection of nucleic acids with as few as ten base pairs, as well as the discrimination of short nucleic acids of similar molecular weights based on differences in their physical dimensions. We take advantage of the single-molecule sensitivity of such nanopores to develop a method for miRNA-specific detection, based on the high affinity and selectivity of the viral p19 protein for 21–22-bp RNA duplexes. We validate our assay by measuring miR122a from rat liver RNA. MiR122a is a relatively abundant, liver-specific miRNA involved in cholesterol biosynthesis, hepatocarcinomas and hepatitis C virus replication<sup>33–35</sup>. We also demonstrate the specificity of our method by showing that miR153, a miRNA not present in liver, is not detected.

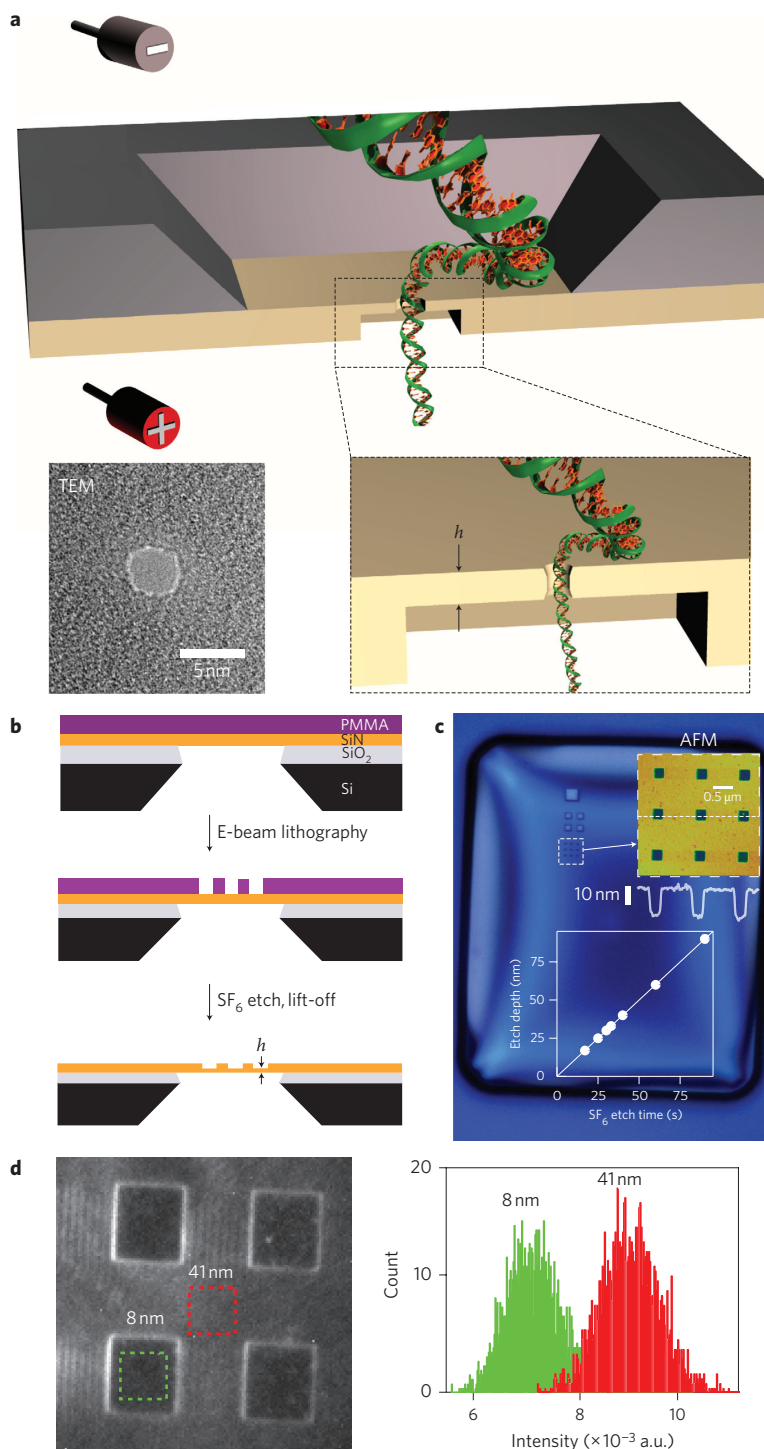
## Nanopores in sub-10-nm-thick SiN membranes

Figure 1a shows our thin solid-state molecular counter. A small region of a freestanding SiN membrane supported by a silicon chip is thinned, after which a nanopore is fabricated using a transmission electron microscope (TEM). Biomolecular translocations through the nanopore appear as transient reductions in the ion current. A TEM image of a 4-nm-diameter pore in a 6-nm-thick membrane is also shown.

The reduction of membrane thickness  $h$  is described in Fig. 1b (see Supplementary Section SI-1 for details). Figure 1c shows an optical micrograph of a processed membrane, in which a pattern of 1, 4 and 9 squares of different sizes has been exposed and etched. An atomic force microscopy (AFM) image of the thinned  $3 \times 3$  array is shown in the top inset. Knowledge of the initial membrane thickness and the etch depth allows the resulting membrane thickness to be calculated. AFM characterization of the depth versus etch time reveals an etch rate of  $1.0 \text{ nm s}^{-1}$  (see Fig. 1c, bottom inset; Supplementary Section SI-2). We also measured the intrinsic fluorescence of SiN membranes from embedded nanosilicon structures<sup>36</sup>. Figure 1d shows that the fluorescence background is reduced in the thinned regions, consistent with a reduced number of fluorescent structures. The thinnest nanopores that were characterized were fabricated in 6-nm-thick membranes (Fig. 3d), and were comparable in thickness to lipid bilayers.

<sup>1</sup>Department of Physics and Astronomy, University of Pennsylvania, Philadelphia Pennsylvania, USA, <sup>2</sup>New England Biolabs, Ipswich, Massachusetts, USA;

<sup>†</sup>These authors contributed equally to this work. \*e-mail: drndic@physics.upenn.edu; wanunu@sas.upenn.edu



**Figure 1 | Solid-state nanopore sensors with a thickness of less than 10 nm.** **a**, Scheme of a nanopore sensor showing a DNA molecule translocating through the pore (not to scale). The sensor consists of a  $5 \times 5 \text{ mm}^2$  silicon chip that contains a free-standing SiN membrane ( $\sim 50 \times 50 \mu\text{m}^2$ ). After locally thinning the membrane using the process shown in **b**, a nanopore is drilled using a TEM (bottom left, image of a 4-nm-diameter nanopore in 6-nm-thick membrane). Electrolyte solution is added above and below the nanopore, each contacted by a Ag/AgCl electrode, and voltage is applied to drive charged biomolecules through the pore. **b**, The membrane thinning process, involves coating the membrane with a PMMA resist, followed by electron-beam exposure and development, and controlled dry etching using  $\text{SF}_6$  plasma. **c**, Optical image of the membrane after thinning (before removal of the PMMA). The upper inset shows an AFM topography image of a  $3 \times 3$  square array following PMMA removal, as well as a line profile that shows uniform, 17-nm-deep trenches. The lower inset shows that the etch depth, measured by AFM, is a linear function of the etch time and that the etch rate is  $1 \text{ nm s}^{-1}$ . **d**, Epi-fluorescence image of a 41-nm-thick SiN membrane in which  $5\text{-}\mu\text{m}$  squares were thinned to 8 nm ( $\lambda_{\text{ex}} = 488 \text{ nm}$ ,  $\lambda_{\text{em}} = 525 \pm 25 \text{ nm}$ ). The fluorescence intensity histograms show that the fluorescence background is lower in the thinned region.

To characterize the sub-10-nm-thick nanopores, bright-field (BF) and annular dark-field (ADF) scanning transmission electron microscopy (STEM) images of a 4.5-nm-diameter pore in a 7-nm-thick

membrane were taken (Fig. 2). Both BF and ADF STEM provide contrast that is very sensitive to membrane thickness. In BF-STEM, the thinned membrane region is a brighter area. The

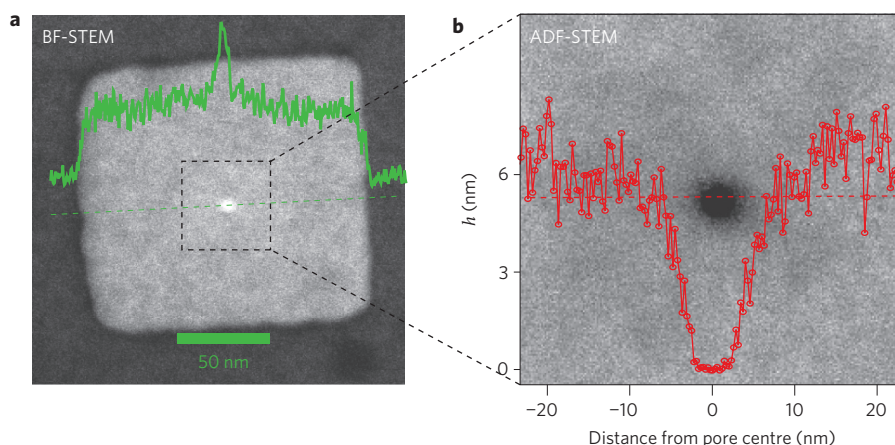


**Figure 2 | Characterization of a 4.5-nm-diameter pore in a 7-nm-thick silicon nitride membrane.** **a**, BF-STEM image, showing the etched  $250 \times 250$  nm square as a brighter area with uniform intensity. **b**, ADF-STEM image of a zoomed-in portion of the nanopore in **a**. The height profile of a line through the centre of the pore is shown by the red line. Membrane thickness  $h$  (y-axis) was measured from the difference of the initial membrane thickness and the etch depth (see text), normalized by assigning a thickness of 0 nm to the signal intensity at the pore (that is, in vacuum). STEM probe size, 0.2 nm.

uniformity of the etched region is indicated by the line profile intensity (green line). A zoomed-in ADF-STEM image reveals a sharp drop in the intensity near the pore (see red line). The contrast is reversed from BF to ADF, so that the pore appears dark.

Based on previous TEM and ion conductance measurements<sup>37,38</sup> and our ADF-STEM measurements, nanopore shapes deviate from a perfect cylinder. However, a simplified geometric model using an equivalent cylinder of reduced thickness and equal diameter to the measured pore diameter can quantitatively explain our data. We define this reduced thickness as the effective pore thickness  $h_{\text{eff}}$ , as illustrated in Fig. 3a (ref. 37).

To a first approximation,  $h_{\text{eff}}$  can be used to quantitatively explain electrolyte transport through the pore. Systematically changing the membrane thickness  $h$  by controlled thinning should have a predictable influence on electrolyte transport through a pore fabricated in such a membrane. When a voltage  $V$  is applied, the ion current  $I_0$  through a cylindrical pore with diameter  $d$  and thickness  $h_{\text{eff}}$  is approximated in high ionic strength solutions ( $>100$  mM) by

$$I_0 = V([\mu_{\text{K}^+} + \mu_{\text{Cl}^-}]n_{\text{KCl}}e) \left( \frac{4h_{\text{eff}}}{\pi d^2} + \frac{1}{d} \right)^{-1} \quad (1)$$

where  $\mu$  is the electrophoretic mobility of a species,  $n_{\text{KCl}}$  the number density of KCl and  $e$  the elementary charge. We modified this equation from earlier works<sup>37,39</sup> to include the access resistance<sup>40,41</sup>, which dominates the conductance in the limit of  $h_{\text{eff}} \rightarrow 0$ . Passage of analytes through the pore transiently reduces the ion current because the ion flux is hindered. Therefore, for pores of similar diameter, reducing the pore thickness should yield two experimental outcomes, increased  $I_0$  (see equation (1)) and increased difference  $\Delta I$  between the open pore current and the current upon occlusion with biomolecules.

To test this, we used similar TEM conditions to fabricate dozens of 4-nm-diameter pores in membranes with  $h = 6$ –60 nm. Figure 3a shows a set of  $\sim 200$  concatenated translocations of 3-kb linear double-stranded DNA (dsDNA) molecules for 4-nm-diameter pores of different thicknesses, recorded at 21 °C and 300 mV. Upon decreasing  $h$ , we find that (i) open pore currents increase and (ii) amplitudes of the DNA translocation signals increase. Decreasing  $h$  vastly improves the signal from biomolecules, as illustrated by the close-up view of representative events in Fig. 3b. All-point current histograms from the traces shown in Fig. 3a are plotted on a semi-logarithmic scale in Fig. 3c. The histograms

were normalized by subtracting the mean open pore current ( $I_0$ ) from each distribution. As predicted, the most probable current amplitude  $\Delta I_p$  (dashed white lines) increases as  $h$  decreases. Also, the broadness of the  $\Delta I$  distributions is augmented in thinner pores. Broad  $\Delta I$  distributions were previously observed for pores in lipid bilayers<sup>42,43</sup> and solid-state membranes<sup>44</sup>, and are probably a result of the varying transport speeds, interactions and/or initial configurations of each molecule before translocation (ref. 45).

Figure 3d shows plots of the experimental mean open-pore currents ( $I_0$ ) (black circles) and the most probable DNA current amplitudes  $\Delta I_p$  (red triangles). Both quantities increase with decreasing  $h$ . The dashed black line is a fit of  $\langle I_0 \rangle$  based on equation (1), where  $h_{\text{eff}}$  is a fitting parameter. Using  $d = 4.0$  nm,  $\mu_{\text{K}^+} = 6.95 \times 10^{-8}$  m<sup>2</sup> V<sup>-1</sup> s<sup>-1</sup>, and  $\mu_{\text{Cl}^-} = 7.23 \times 10^{-8}$  m<sup>2</sup> V<sup>-1</sup> s<sup>-1</sup> (ref. 46), a best fit to our data is obtained using  $h_{\text{eff}} = h/(3.04 \pm 0.30)$ , in good agreement with previous measurements for thicker membranes (see top  $x$ -axis of Fig. 3d)<sup>37</sup>. Based on the fit, the thinnest pores we show here with  $h = 6$  nm have a calculated  $h_{\text{eff}}$  of 2 nm.

To fit the experimental  $\Delta I_p$  values, we used a geometric model to compute the residual current through the pore when occupied by a DNA strand (Supplementary Section SI-4). In this model, dsDNA is assumed to be a cylinder with a diameter of 2.2 nm, and  $\Delta I$  is computed from the unobstructed area of the DNA-occluded pore. We also add to this model a parameter  $S$  that describes the fraction of chloride ions excluded from the nanopore vicinity by the highly charged DNA coil. A previous report that  $\Delta I$  increases as a function of DNA length in 4-nm pores<sup>44</sup> suggests that the highly charged DNA coil excludes Cl<sup>-</sup> from the pore vicinity, therefore reducing [Cl<sup>-</sup>] near the pore. Using a single parameter of  $20 \pm 5\%$  Cl<sup>-</sup> exclusion for 3-kb DNA, our results match the model for  $\Delta I$  (equation (2) in Supplementary Section SI-4) for all tested  $h_{\text{eff}}$  values (see dashed red curve). The inset to Fig. 3d shows the experimental (markers) and calculated (dashed green line) blockage fractions  $\Delta I_p/\langle I_0 \rangle$  as a function of  $h$ . In the regime where access resistance does not dominate (that is, for  $h > 10$  nm),  $\Delta I_p/\langle I_0 \rangle$  is independent of  $h$ .

Figure 3e displays signal-to-noise ratios  $S/N = \Delta I_p/I_{\text{rms}}$  as a function of  $h$ , where  $I_{\text{rms}}$  is the open-pore current (root mean square, r.m.s.) at a bandwidth of 100 kHz. We find that  $I_{\text{rms}}$  is independent of  $h$  ( $I_{\text{rms}} \approx 70$ –80 pA at a bandwidth of 100 kHz), which results in increasing  $S/N$  values with decreasing  $h$ , because  $\Delta I$  increases with decreasing  $h$ . We obtain  $S/N = 46$  for  $h = 6$  nm, a marked improvement over  $S/N \approx 10$  in similar-diameter pores with  $h = 25$  nm (ref. 47).

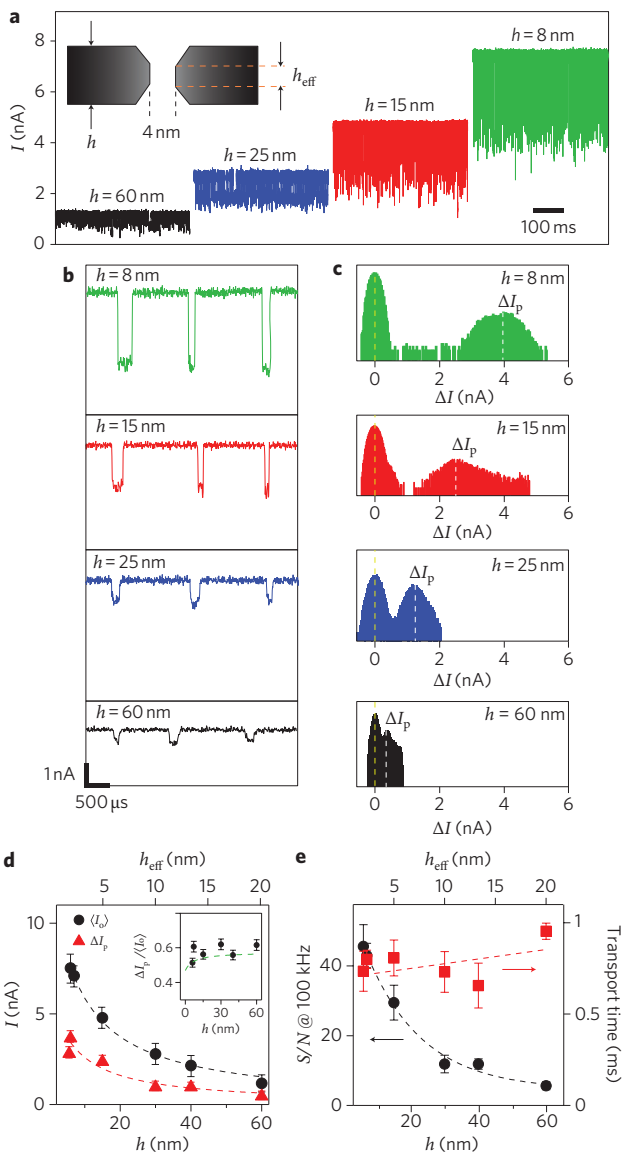


**Figure 3 | Increasing the measurement resolution by nanopore thinning.** **a**, Concatenated sets of  $\sim 200$  translocations of 3-kb linear dsDNA through 4-nm-diameter pores fabricated in membranes with different  $h$  values;  $h_{\text{eff}}$  is the nanopore effective thickness used in the geometric model discussed in the text. On decreasing  $h$  from 60 to 6 nm, the open-pore current increased and the DNA signal amplitude increased. All traces were filtered using the Axopatch 100 kHz filter setting. For  $h = 60$  nm, the data was low-pass filtered at 10 kHz using the Axopatch filter to make events visible. **b**, Magnified view of the traces in **a**. **c**, Semi-logarithmic histograms of the blocked current amplitudes normalized by subtracting  $\Delta I$ , which show increased current amplitudes for thinner nanopores. Although the most probable blocked current  $\Delta I_p$  increased with decreasing  $h$ , open-pore noise values were similar. **d**, Dependence of average experimental  $\langle I_0 \rangle$  (black circles) and the most probable DNA current amplitude  $\Delta I_p$  (red triangles) on  $h$ . The black dashed line is a fit using equation (1) to the average  $I_0$  data from the combined data of  $\sim 20$  pores, which yields an effective pore thickness  $h_{\text{eff}} = h / (3.04 \pm 0.30)$  ( $h_{\text{eff}}$  scale shown on top x-axis). The fit to  $\Delta I_p$  values (red dashed line) is based on a geometric model described in detail in Supplementary Section SI-4. Inset shows  $\Delta I_p / \langle I_0 \rangle$ , which did not change appreciably with  $h$ . The green dashed line is the ratio of the fits to  $\Delta I_p$  and  $\langle I_0 \rangle$  from the main plot. **e**,  $S/N$  and mean transport time as a function of  $h$  ( $h_{\text{eff}}$  shown on top x-axis).  $S/N$  is defined as  $\Delta I / I_{\text{rms}}$ , where  $I_{\text{rms}}$  at 100 kHz bandwidth is  $75 \pm 5$  pA. Mean transport times were obtained from the dwell-time distributions (see ref. 47 for more details).

Finally, a potential concern in this study was that reducing  $h$  would also reduce DNA interactions with the pore surface, thereby speeding up DNA transport and presenting detection challenges. The right axis of Fig. 3e shows that the mean transport times for the 3-kb DNA molecules are approximately independent of  $h$ , with less than 30% decrease in transport times when  $h$  is reduced from 60 to 6 nm (Supplementary Section SI-5). The weak dependence of transport times on  $h$  indicates that parameters other than surface interactions (for example, electro-osmotic drag<sup>48,49</sup>), influence the transport dynamics.

**Discrimination between small nucleic acids.** Using the increased signal amplitude in thin nanopores, we tested the ability of a thin pore ( $d = 3$  nm,  $h = 7$  nm) to discriminate between small nucleic acids. We first compared 22-bp RNA and 25-bp DNA, because the two molecules have similar effective solvation volumes ( $\sim 35$  nm<sup>3</sup> and  $\sim 32.3$  nm<sup>3</sup>, respectively) and molecular weights ( $\sim 15$  kDa), while differing in cross-sectional areas by  $\sim 35\%$  due to their different helicities (see in Fig. 4a PDB files 1RPU and 2BNA from <http://www.rcsb.org>). Continuous current traces, as well as magnified sets of representative events are shown in Fig. 4a. To quantify the difference between the molecular signatures, we also show all-point current histograms for DNA (blue) and RNA (red), which highlight the characteristic signal from longer events. The histograms reveal peaks at characteristic current amplitudes of  $\Delta I_{\text{DNA}} = 0.54$  nA and  $\Delta I_{\text{RNA}} = 0.92$  nA. Similar amplitudes were obtained for 10-bp DNA and 25-bp DNA, although the 10-bp molecule often stuck to the pore for timescales  $> 1$  ms because the 10-bp molecule is comparable in length to the pore dimensions (Supplementary Section SI-6).

The difference in current amplitudes between short DNA and RNA is  $\sim 40\%$ , in good agreement with their cross-sectional area differences<sup>24</sup>. The mean transport times for the RNA molecule (50  $\mu$ s) were significantly longer than those for the DNA molecule (20  $\mu$ s). This, in addition to a broader  $\Delta I$  distribution for RNA, is probably a result of drag forces on the wider helical structure of RNA, and a greater level of interactions between RNA and the nanopore. Note that differences in current amplitudes between DNA and RNA persist even for events with durations  $\leq 16$   $\mu$ s, for which the signal amplitude is attenuated by as much as 20% due to our use of a rank 1 median filter (Supplementary Section SI-7). Using a discrimination threshold of  $\Delta I_{\text{thres}} = 675$  pA, we can discern DNA from RNA with  $> 97\%$  certainty by considering events with durations of  $\geq 16$   $\mu$ s, which represent  $> 75\%$  of the total detected events. Analysis of events with durations of  $\leq 16$   $\mu$ s shows that the signal is attenuated by the same factor for both DNA and RNA, enabling discrimination even for events with this duration range (Supplementary Section SI-7). We have also checked that discrimination based on  $\Delta I$  is not a result of the faster mean transport times for DNA by comparing events for DNA and RNA with similar durations, in which we see  $< 10\%$  overlap in the two  $\Delta I$  distributions (Supplementary Section SI-7).

The pores could also distinguish linear nucleic acids from more complex structures. For example, transfer-RNA (tRNA) is structurally more complex than duplex RNA and DNA because of the presence of unpaired bases and loops, which give rise to a bent structure (see in Fig. 4a the structure of phenylalanine tRNA from PDB file 4TNA). The black trace in Fig. 4a shows events with amplitudes of 1.8 nA for the tRNA, a factor of two greater than for the 22-bp RNA molecule (0.92 nA). The mean transport time of the tRNA molecule is 1.04 ms, much longer than that of the linear nucleic acids (Supplementary Section SI-7 and expanded events in Fig. 4a). These differences in signal between the three molecules show that we can discriminate among populations of the three nucleic acids with good certainty. Despite this, the current amplitudes for the short DNA and RNA molecules are significantly

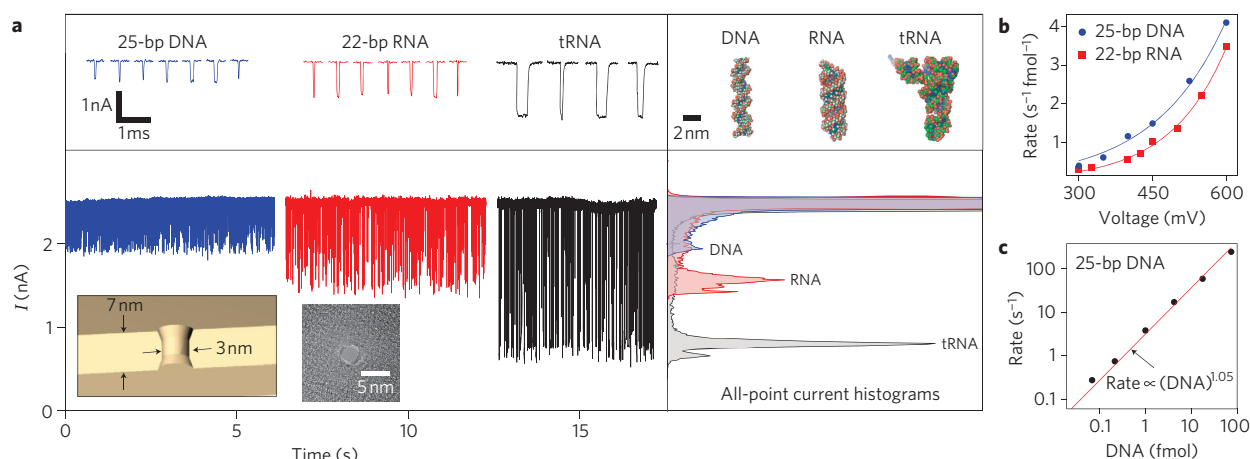


**Figure 4 | Discrimination among small nucleic acids using thin nanopores.** **a**, Continuous current versus time traces from a 3-nm-diameter pore in a 7-nm-thick membrane measured at 0 °C,  $V = 500$  mV (TEM image of pore is shown). Traces were median-filtered with rank of 1 to improve the S/N. Based on the conductance, the effective pore thickness  $h_{\text{eff}} = 2.3$  nm. The analyte chamber contains 25-bp dsDNA (blue), 22-bp dsRNA (red) or phenylalanine tRNA (black), at concentrations of  $\sim 80$  fmol  $\mu\text{l}^{-1}$ . Sample events are shown above the continuous traces, and models based on crystal structures are shown to the right. The all-point current histograms on the bottom right show that the three molecules can be distinguished based on their current amplitudes. The mean transport times for the DNA, RNA and tRNA molecules are 20  $\mu\text{s}$ , 50  $\mu\text{s}$  and 1.04 ms, respectively (Supplementary Section SI-7). **b**, Dependence of the capture rate on the applied voltage for 25-bp DNA and 22-bp RNA. The exponential dependence reveals that capture is voltage-activated. Blue and red lines are exponential fits to the data. **c**, Log-log plot of capture rate versus DNA concentration. Linearity is observed for three orders of magnitude in DNA concentration, as indicated by a power-law fit exponent of  $1.05 \pm 0.03$ .

lower than our simple geometric model predicts (Supplementary Section SI-4), suggesting that a more detailed model is required to quantitatively describe ion blockade amplitudes of small nucleic acids.

Figure 4b shows mean capture rates versus voltage for 25-bp DNA and 22-bp RNA (see Supplementary Section SI-8 for traces). The mean capture rates are exponentially dependent on voltage in the range 300–600 mV (red and blue curves are exponential fits to the data), suggesting that nucleic acid capture is a voltage-activated process. Based on the ratio of the observed event rate and the calculated arrival rate of molecules to the pore at 600 mV (ref. 47), we estimate that  $>50\%$  of the molecules that arrive at the pore are captured and detected.

The concentration of a sample can be measured from the frequency of molecular signals, provided that a calibration curve of capture rate versus concentration is constructed. In Fig. 4c, a log-log plot of the mean capture rate versus concentration of 25-bp DNA is shown (Supplementary Section SI-9). The power-law fit to the data (red line) yields an exponent of  $1.05 \pm 0.03$ , indicating linearity over three orders of magnitude in concentration. This dynamic range can be extended by orders of magnitude by increasing the measurement time and applied voltage, or by adjusting the electrostatic potential at the pore entrance<sup>47,50,51</sup>.

### Electronic platform for detection of specific miRNAs

Electronic detection of small RNAs using a solid-state device may provide a low-cost, attractive alternative to existing methods for rapid and sensitive miRNA analysis. Microarray-based miRNA profiling<sup>52</sup>, fluorescence<sup>53</sup>, radioactive gel electrophoresis and other novel techniques can detect subfemtomole RNA levels, but none of these offers the unique features of nanopore detection, such as electronic sensing, single-molecule sensitivity, reusability, use of an unlabelled probe and avoidance of surface immobilization. To detect a specific miRNA with a nanopore, a sequence-specific enrichment step of a particular miRNA is required, because concentrations of miRNAs are  $<1\%$  relative to other cellular RNAs.

To enrich a specific RNA, the p19 protein from the Carnation Italian ringspot virus was used. P19 binds 21–23-bp dsRNA in a

size-dependent, but sequence-independent manner<sup>54</sup>. The protein does not bind ssRNA, tRNA or rRNA (ref. 55). To enhance isolation of the bound dsRNA we created a C-terminal fusion of p19 with the chitin-binding domain (CBD), allowing linkage of the p19 fusion protein to chitin magnetic beads<sup>55</sup>. The magnetic beads simplify the washing steps required to remove unbound RNA. Using p19 beads we have achieved over 100,000-fold enrichment of the probe:miRNA duplex from total RNA. We developed the protocol shown in Fig. 5a for nanopore-based miRNA detection. It begins with isolation of total RNA from tissue and hybridization to a miRNA-specific oligonucleotide RNA probe complementary to a target miRNA. In step (I), the probe-hybridized total RNA is incubated with the p19 protein immobilized on magnetic beads, followed by washing to remove the remaining RNA. In step (II), the purified probe:miRNA duplex is eluted from the p19 protein. In step (III), the duplex is detected using a nanopore (see Supplementary Section SI-11 for details). A typical miRNA enrichment protocol takes several hours, starting from isolated cellular RNA.

MiRNAs isolated with p19 may contain agents that interfere with nanopore detection of the probe:miRNA duplex. Together with the eluted duplex, other agents may be present, such as bovine serum albumin (BSA), which coats the beads, sodium dodecyl sulphate (SDS), used for dsRNA elution from the p19, and trace amounts of other RNAs. To eliminate the possibility of an artefact signal being caused by these interfering agents, several controls were performed. The results are summarized in Fig. 5b, which shows 30-s current traces for different samples, all of which have been treated using p19 beads. The first trace shown in red is for the probe:miR122a duplex reacted with 1  $\mu\text{g}$  rat liver RNA (RL). The second trace shown in blue is for a positive control (PC), in which 30 ng of synthetic probe:miR122a duplex was bound to and eluted from p19 beads. In addition to the positive control samples, we performed four negative controls NC1 to NC4, which are described in the Methods. The traces show spikes with current amplitudes as expected from dsRNA for samples PC and RL, whereas no spikes of amplitudes greater than 0.3 nA were present in the four negative controls. The open-pore current was stable to within 5% throughout the experiments.

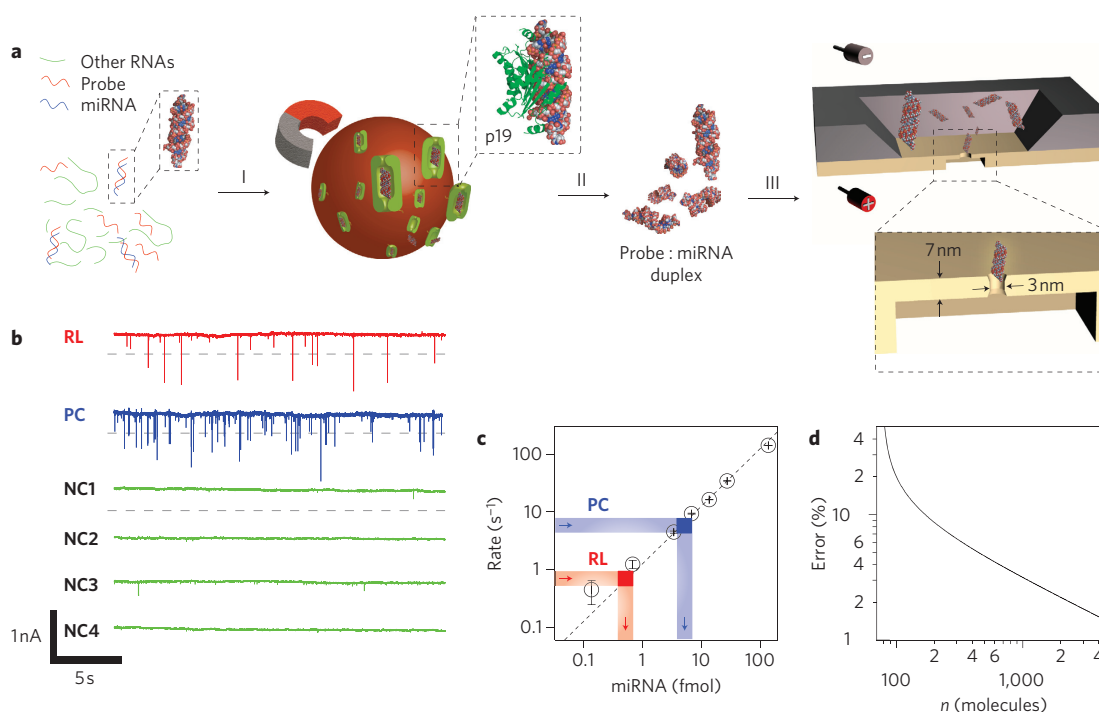


**Figure 5 | miRNA detection using solid-state molecular counters.** **a**, Scheme of the miRNA-specific detection method. First, RNA is extracted from tissue (not shown), and the extract is hybridized to a miRNA-specific oligonucleotide probe (red). In step (I), the probe:miRNA duplex is enriched by binding to p19-functionalized magnetic beads, followed by thorough washing to remove other RNAs from the mixture. In step (II), the hybridized probe:miRNA duplex is eluted from the magnetic beads. In step (III), the eluted probe:miRNA duplex is electronically detected using a nanopore. **b**, Detection of miR122a from 1  $\mu\text{g}$  of rat liver total RNA using a 3-nm-diameter nanopore in a 7-nm-thick membrane. Representative 30-s current versus time traces are shown for a pore after the addition of the enriched miR122a (RL), a positive control containing a synthetic miR122a RNA duplex bound to magnetic beads, followed by washing, elution and detection (PC), and four different negative controls (NC1–NC4, see Methods). The negative controls did not produce any signal below the threshold, which was set to  $\langle I_{\text{off}} \rangle - 0.4$  nA (see dashed grey lines in Fig. 5b). **c**, Quantification of miR122a from the mean capture rates. A calibration curve of capture rate versus concentration was constructed (dashed black line) using different concentrations of synthetic 22-bp RNA duplex, showing that capture rate scales linearly with concentration over three orders of magnitude. Determination of miR122a amounts (per  $\mu\text{l}$  solution) is based on the spike rate for sample RL (thick red lines) and the positive control PC (thick blue lines). **d**, Relative error in the determined RNA concentration as a function of the number of molecules counted by the nanopore (see text). To achieve 93% accuracy under our conditions, the time required for determination of 1 fmol RNA sample is 4 min, corresponding to  $\sim 250$  spikes.

To quantify the miRNA concentration, a calibration curve of capture rate versus concentration was first constructed using a synthetic probe:miR122a duplex, indicated by the open symbols in Fig. 5c (see Supplementary Section SI-10 for current traces at different duplex concentrations). For an unknown miRNA sample, we then counted  $\sim 250$  current spikes that crossed the threshold of  $\langle I_{\text{off}} \rangle - 0.4$  nA (see dashed grey lines in the traces in Fig. 5b), computed the mean capture rate, and used the calibration curve to determine the RNA concentration. The red and blue lines in Fig. 5c show how the capture rates translate to RNA concentration for samples RL and PC, respectively. From the calibration curve, the concentration of the 20-fold diluted miR122a in sample RL is  $0.7 \text{ fmol } \mu\text{l}^{-1}$ , translating to an original abundance of  $78 \pm 2 \text{ pg miR122a}/\mu\text{g liver RNA}$  in rat liver cells, in close agreement with previous findings ( $58\text{--}67 \text{ pg miR122a}/\mu\text{g RNA}$ )<sup>52</sup>. In addition, sample PC showed the expected concentration of  $5.2 \text{ fmol } \mu\text{l}^{-1}$ , indicating that the synthetic probe:miR122a duplex efficiently bound to and eluted from the p19 beads. The negative controls did not show any current spikes that crossed the threshold over the measurement time (2 min each), indicating a background that is at least two orders of magnitude lower in spike frequency than sample RL (that is, background noise  $< 7 \text{ amol } \mu\text{l}^{-1}$ ).

Figure 5d shows the relative error in measured concentration versus the number of detected molecules. The plot was generated by computing the standard error in the mean capture rates for population subsets of sizes ranging from 100 to 4,000 events.

Based on Fig. 5c and d, one can obtain the time required to analyse a sample with a desired accuracy. For 1 fmol miRNA duplex per  $\mu\text{l}$  solution, the capture rate is  $\sim 1 \text{ molecule s}^{-1}$ , so detection of 250 molecules in  $\sim 4$  min is sufficient to determine miRNA concentration with 93% certainty.

In conclusion, we have developed a process for fabricating uniform, robust and well-defined solid-state membranes that can be manufactured on a full silicon wafer, and used it to make solid-state nanopore sensors with the thickness of lipid membranes. Reducing the nanopore thickness improves the signal amplitude from biomolecules, and the use of 3-nm pores in sub-10-nm membranes facilitates electronic discrimination among small nucleic acids. Moreover, nanopores in thin membranes are more easily hydrated than nanopores in thicker membranes, and remain stable over time. Three types of small nucleic acids with different structures were discriminated with good signal contrast. The systematic study of thin nanopore properties has allowed us to develop an electronic detection process for counting individual small RNA molecules, which we have used to quantify miRNA enriched from biological tissue. The inherent ability of our system to electronically detect single molecules, combined with microfluidic-scale sample volumes (nl), has the potential to exceed the detection limits of conventional methods. We anticipate the simultaneous detection of different molecular species in solution (peptides, miRNA and so on) by the multiplexed readout of electronic signals from many pores.

## Methods

The substrates for device fabrication were  $5 \times 5 \text{ mm}^2$  silicon chips with a low-stress SiN film deposited on a  $5\text{-}\mu\text{m}$ -thick thermally grown  $\text{SiO}_2$  layer, which was used to reduce the electrical noise. Electron-beam lithography was used to write square patterns on the membranes, followed by developing the exposed areas and locally thinning the SiN membrane using an  $\text{SF}_6$  plasma etcher. After lift-off of the resist and hot piranha cleaning, AFM was used to profile the etch depth (Enviroscope, Veeco). Epi-fluorescence was measured using an upright microscope (Nikon Eclipse 80i) with a Nikon Apo  $100 \times 0.95 \text{ NA}$  dry objective. Laser excitation at  $488 \text{ nm}$  was blocked using a notch filter and detected behind a Chroma 525/50 emission filter using a cooled charge-coupled device (Princeton Instruments). Solid-state nanopores were fabricated and analysed in a JEOL 2010FEG TEM equipped with an annular detector for ADF-STEM. The resulting geometry of nanopores fabricated in solid-state membranes is governed by an interplay between surface tension of the molten SiN and its ablation kinetics<sup>17</sup>. Adjustment of the pore shape by tuning the electron-beam fabrication process has been previously reported<sup>17,37,38,56</sup>. In light of a recent report that the TEM beam size influences nanopore shape<sup>57</sup>, we used an intense electron-beam spot with a diameter of  $1\text{--}2 \text{ nm}$  to drill our nanopores. All nanopore experiments were carried out using  $1 \text{ M KCl} + 1 \text{ mM EDTA}$ , Tris buffered to  $\text{pH } 8$ . Our fluoropolymer cell accommodates volumes of  $1\text{--}20 \mu\text{l}$  and features temperature regulation using a thermoelectric device. The nanopore chip was installed between two buffered electrolyte solutions, each equipped with an Ag/AgCl electrode. After piranha cleaning, each chip was installed in a custom fluoropolymer cell that accommodated volumes as small as  $1 \mu\text{l}$ . The fraction of pores that yielded a steady ion conductance in good agreement with equation (1) using  $h_{\text{eff}} = h/3$  was  $\sim 100\%$  for  $h < 10 \text{ nm}$ , compared to  $40\text{--}60\%$  for similarly treated pores with  $h = 25 \text{ nm}$ . Presumably, this result reflects the reduced capacity of thinner pores for trapping hydrophobic contaminants. Pores that exhibited fluctuating currents characterized by high  $1/f$  noise and conductance less than  $2 \text{ nS}$  were not reported in Fig. 3d and were re-cleaned. When the electrolyte chamber was sealed using a polydimethylsiloxane (PDMS) gasket, or when the cell temperature was reduced to  $< 10^\circ \text{C}$ , the conductance of pores with different thicknesses was stable to within  $5\%$  for hours (Supplementary Section SI-3). For translocation experiments, analyte was added to one of the chambers, and voltage was applied while monitoring current through the pore. Electrical current, measured using an Axopatch 200B amplifier, was digitized at  $250 \text{ kHz}$  and fed to a computer using custom LabVIEW collection/analysis software. For short nucleic acid analysis we digitally filtered the data using a median filter with a rank of 1, for which we found that events with durations of  $\geq 24 \mu\text{s}$  were undistorted (see Supplementary Section SI-7 and Supplementary Appendix A). All DNA samples were purchased from Fermentas (NoLimits). For the experiments in Fig. 3,  $4.0 \pm 0.2 \text{ nm}$  pores were used,  $\sim 1 \text{ nM}$  DNA concentrations were placed in one chamber at  $21 \pm 0.1^\circ \text{C}$ , and  $300 \text{ mV}$  was applied to the opposite chamber. The miR122a probe was a 22-nucleotide complementary RNA to miR122a with two-nucleotide 3' extension, phosphorylated at the 5' terminus ( $5'\text{-AACACCAUUGUCACACUCCAUA-3}'$ ). The probe:miRNA duplex was enriched from RNA using the protocol in Supplementary Section SI-10. For miRNA determination,  $\sim 1 \mu\text{l}$  sample was added to the negative chamber of a  $3\text{-nm}$  nanopore in a  $7\text{-nm}$ -thick membrane, and current was recorded versus time at  $500 \text{ mV}$  and  $0^\circ \text{C}$ . (See Supplementary Section SI-10 for more details about the experiment in Fig. 5.) In the first negative control (NC1),  $1 \mu\text{g}$  of liver RNA was hybridized to a non-specific miRNA probe for miR153 ( $5'\text{-CACUUUGUGACUAUGCAA-3}'$ ), which is absent in liver<sup>52</sup>. In the second negative control (NC2), no probe was hybridized to  $1 \mu\text{g}$  of liver RNA. In the third negative control (NC3), miR122a probe was hybridized to yeast RNA, which does not contain miR122a. In the fourth negative control (NC4), single-stranded miR122a was incubated without any other RNA. In equation (1) in our geometrical model, we neglected the low SiN surface charge density<sup>47</sup> because experiments were performed at high ionic strengths ( $1 \text{ M KCl}$ ).

Received 28 May 2010; accepted 14 September 2010;  
published online 24 October 2010

## References

- Lee, R. C., Feinbaum, R. L. & Ambros, V. The *C. elegans* heterochronic gene LIN-4 encodes small RNAs with antisense complementarity to LIN-14. *Cell* **75**, 843–854 (1993).
- Carthew, R. W. & Sontheimer, E. J. Origins and mechanisms of miRNAs and siRNAs. *Cell* **136**, 642–655 (2009).
- Winter, J., Jung, S., Keller, S., Gregory, R. I. & Diederichs, S. Many roads to maturity: microRNA biogenesis pathways and their regulation. *Nature Cell Biol.* **11**, 228–234 (2009).
- Fire, A. *et al.* Potent and specific genetic interference by double-stranded RNA in *Caenorhabditis elegans*. *Nature* **391**, 806–811 (1998).
- Whitehead, K. A., Langer, R. & Anderson, D. G. Knocking down barriers: advances in siRNA delivery. *Nature Rev. Drug Discov.* **8**, 129–138 (2009).
- Oh, Y. K. & Park, T. G. siRNA delivery systems for cancer treatment. *Adv. Drug Deliv. Rev.* **61**, 850–862 (2009).
- Singh, S. K. & Hajeri, P. B. siRNAs: their potential as therapeutic agents—part II. Methods of delivery. *Drug Discov. Today* **14**, 859–865 (2009).

- Murphy, J. & Bustin, S. A. Reliability of real-time reverse-transcription PCR in clinical diagnostics: gold standard or substandard? *Expert Rev. Mol. Diagnostics* **9**, 187–197 (2009).
- Coulter, W. H. US patent 2,656,508 (1953).
- Bezrukov, S. M., Vodyanoy, I. & Parsegian, V. A. Counting polymers moving through a single-ion channel. *Nature* **370**, 279–281 (1994).
- Kasianowicz, J. J., Brandin, E., Branton, D. & Deamer, D. W. Characterization of individual polynucleotide molecules using a membrane channel. *Proc. Natl Acad. Sci. USA* **93**, 13770–13773 (1996).
- Gu, L. Q., Braha, O., Conlan, S., Cheley, S. & Bayley, H. Stochastic sensing of organic analytes by a pore-forming protein containing a molecular adapter. *Nature* **398**, 686–690 (1999).
- Butler, T. Z., Pavlenok, M., Derrington, I. M., Niederweis, M. & Gundlach, J. H. Single-molecule DNA detection with an engineered MspA protein nanopore. *Proc. Natl Acad. Sci. USA* **105**, 20647–20652 (2008).
- Wendell, D. *et al.* Translocation of double-stranded DNA through membrane-adapted phi29 motor protein nanopores. *Nature Nanotech.* **4**, 765–772 (2009).
- Howorka, S. & Siwy, Z. Nanopore analytics: sensing of single molecules. *Chem. Soc. Rev.* **38**, 2360–2384 (2009).
- Li, J. *et al.* Ion-beam sculpting at nanometre length scales. *Nature* **412**, 166–169 (2001).
- Storm, A. J., Chen, J. H., Ling, X. S., Zandbergen, H. W. & Dekker, C. Fabrication of solid-state nanopores with single-nanometre precision. *Nature Mater.* **2**, 537–540 (2003).
- Li, J. L., Gershow, M., Stein, D., Brandin, E. & Golovchenko, J. A. DNA molecules and configurations in a solid-state nanopore microscope. *Nature Mater.* **2**, 611–615 (2003).
- Heng, J. B. *et al.* The electromechanics of DNA in a synthetic nanopore. *Biophys. J.* **90**, 1098–1106 (2006).
- Iqbal, S. M., Akin, D. & Bashir, R. Solid-state nanopore channels with DNA selectivity. *Nature Nanotech.* **2**, 243–248 (2007).
- Fologea, D., Ledden, B., McNabb, D. S. & Li, J. L. Electrical characterization of protein molecules by a solid-state nanopore. *Appl. Phys. Lett.* **91**, 053901 (2007).
- Zhao, Q. *et al.* Stretching and unzipping nucleic acid hairpins using a synthetic nanopore. *Nucleic Acids Res.* **36**, 1532–1541 (2008).
- Tabard-Cossa, V. *et al.* Single-molecule bonds characterized by solid-state nanopore force spectroscopy. *ACS Nano* **3**, 3009–3014 (2009).
- Skinner, G. M., van den Hout, M., Broekmans, O., Dekker, C. & Dekker, N. H. Distinguishing single- and double-stranded nucleic acid molecules using solid-state nanopores. *Nano Lett.* **9**, 2953–2960 (2009).
- Kowalczyk, S. W., Hall, A. R. & Dekker, C. Detection of local protein structures along DNA using solid-state nanopores. *Nano Lett.* **10**, 324–328 (2010).
- Smeets, R. M. M., Kowalczyk, S. W., Hall, A. R., Dekker, N. H. & Dekker, C. Translocation of RecA-coated double-stranded DNA through solid-state nanopores. *Nano Lett.* **9**, 3089–3095 (2009).
- Wanunu, M., Sutin, J. & Meller, A. DNA profiling using solid-state nanopores: detection of DNA-binding molecules. *Nano Lett.* **9**, 3498–3502 (2009).
- Singer, A. *et al.* Nanopore based sequence specific detection of duplex DNA for genomic profiling. *Nano Lett.* **10**, 738–742 (2010).
- Branton, D. *et al.* The potential and challenges of nanopore sequencing. *Nature Biotechnol.* **26**, 1146–1153 (2008).
- Garaj, S. *et al.* Graphene as a subnanometre trans-electrode membrane. *Nature* **467**, 190–193 (2010).
- Schneider, G. F. *et al.* DNA translocation through graphene nanopores. *Nano Lett.* **10**, 3163–3167 (2010).
- Merchant, C. A. *et al.* DNA translocation through graphene nanopores. *Nano Lett.* **10**, 2915–2921 (2010).
- Krutzfeldt, J. Silencing of microRNAs *in vivo* with *et al.* 'antagomirs'. *Nature* **438**, 685–689 (2005).
- Bai, S. M. *et al.* MicroRNA-122 inhibits tumorigenic properties of hepatocellular carcinoma cells and sensitizes these cells to sorafenib. *J. Biol. Chem.* **284**, 32015–32027 (2009).
- Lanford, R. E. *et al.* Therapeutic silencing of microRNA-122 in primates with chronic hepatitis C virus infection. *Science* **327**, 198–201 (2010).
- Park, N. M., Choi, C. J., Seong, T. Y. & Park, S. J. Quantum confinement in amorphous silicon quantum dots embedded in silicon nitride. *Phys. Rev. Lett.* **86**, 1355–1357 (2001).
- Kim, M. J., Wanunu, M., Bell, D. C. & Meller, A. Rapid fabrication of uniformly sized nanopores and nanopore arrays for parallel DNA analysis. *Adv. Mater.* **18**, 3149–3155 (2006).
- Wu, M. Y. *et al.* Control of shape and material composition of solid-state nanopores. *Nano Lett.* **9**, 479–484 (2009).
- Smeets, R. M. M. *et al.* Salt dependence of ion transport and DNA translocation through solid-state nanopores. *Nano Lett.* **6**, 89–95 (2006).
- Hall, J. E. Access resistance of a small circular pore. *J. Gen. Physiol.* **66**, 531–532 (1975).
- Vodyanoy, I. & Bezrukov, S. M. Sizing of an ion pore by access resistance measurements. *Biophys. J.* **62**, 10–11 (1992).

42. Akeson, M., Branton, D., Kasianowicz, J. J., Brandin, E. & Deamer, D. W. Microsecond time-scale discrimination among polycytidylic acid, polyadenylic acid and polyuridylic acid as homopolymers or as segments within single RNA molecules. *Biophys. J.* **77**, 3227–3233 (1999).
43. Mathe, J., Aksimentiev, A., Nelson, D. R., Schulten, K. & Meller, A. Orientation discrimination of single-stranded DNA inside the alpha-hemolysin membrane channel. *Proc. Natl Acad. Sci. USA* **102**, 12377–12382 (2005).
44. Wanunu, M., Sutin, J., McNally, B., Chow, A. & Meller, A. DNA translocation governed by interactions with solid-state nanopores. *Biophys. J.* **95**, 4716–4725 (2008).
45. Aksimentiev, A. Deciphering ionic current signatures of DNA transport through a nanopore. *Nanoscale* **2**, 468–483 (2010).
46. Lide, D. R. (ed.) Ionic conductivity and diffusion at infinite dilution, in *CRC Handbook of Chemistry and Physics* (CRC Press, 2005).
47. Wanunu, M., Morrison, W., Rabin, Y., Grosberg, A. Y. & Meller, A. Electrostatic focusing of unlabelled DNA into nanoscale pores using a salt gradient. *Nature Nanotech.* **5**, 160–165 (2010).
48. Luan, B. Q. & Aksimentiev, A. Electro-osmotic screening of the DNA charge in a nanopore. *Phys. Rev. E* **78**, 4 (2008).
49. van Dorp, S., Keyser, U. F., Dekker, N. H., Dekker, C. & Lemay, S. G. Origin of the electrophoretic force on DNA in solid-state nanopores. *Nature Phys.* **5**, 347–351 (2009).
50. Gu, L. Q., Cheley, S. & Bayley, H. Electroosmotic enhancement of the binding of a neutral molecule to a transmembrane pore. *Proc. Natl Acad. Sci. USA* **100**, 15498–15503 (2003).
51. Kasianowicz, J. J., Nguyen, T. L. & Stanford, V. M. Enhancing molecular flux through nanopores by means of attractive interactions. *Proc. Natl Acad. Sci. USA* **103**, 11431–11432 (2006).
52. Bissels, U. *et al.* Absolute quantification of microRNAs by using a universal reference. *RNA* **15**, 2375–2384 (2009).
53. Foldes-Papp, Z. *et al.* Trafficking of mature miRNA-122 into the nucleus of live liver cells. *Curr. Pharm. Biotechnol.* **10**, 569–578 (2009).
54. Vargason, J. M., Szittyá, G., Burgyan, J. & Hall, T. M. T. Size selective recognition of siRNA by an RNA silencing suppressor. *Cell* **115**, 799–811 (2003).
55. Jin, J., Cid, M., Poole, C. B. & McReynolds, L. A. Protein-mediated miRNA detection and siRNA enrichment using p19. *Biotechniques* **48**, 17–23 (2010).
56. Wu, M. Y., Krapf, D., Zandbergen, M., Zandbergen, H. & Batson, P. E. Formation of nanopores in a SiN/SiO<sub>2</sub> membrane with an electron beam. *Appl. Phys. Lett.* **87**, 113106 (2005).
57. van den Hout, M. *et al.* Controlling nanopore size, shape and stability. *Nanotechnology* **21**, 115304 (2010).

### Acknowledgements

The authors would like to thank M. Fischbein for assistance with optimizing the plasma etch process, the laboratory of C. Johnson for the use of their plasma etcher, D. Yates for assistance with ADF-STEM, and G. Rosenbloom and B. Cooperman for the tRNA molecule. The authors also thank J. Bartel, J. Fairfield, M. Goulian, K. Healy, R. Johnson, C. Johnson, N. Peterman, G.V. Soni and L. Willis for helpful advice regarding the manuscript. This work was supported by the National Institutes of Health (grant no. R21HG004767) and the Penn Genomics Frontier Institute. T.D. acknowledges support from the Israel Science Foundation (Bikura postdoctoral fellowship).

### Author contributions

M.W. and L.M. conceived and designed the experiments. T.D., V.R. and M.W. designed, fabricated and characterized the nanopore devices. J.J. and L.M. developed and performed the miRNA enrichment protocols. M.W. performed the nanopore experiments and analysed the data. M.W., T.D., L.M. and M.D. wrote the manuscript, and all other authors commented on it.

### Additional information

The authors declare competing financial interests: details accompany the full-text HTML version of the paper at [www.nature.com/naturenanotechnology](http://www.nature.com/naturenanotechnology). Supplementary information accompanies this paper at [www.nature.com/naturenanotechnology](http://www.nature.com/naturenanotechnology). Reprints and permission information is available online at <http://npg.nature.com/reprintsandpermissions/>. Correspondence and requests for materials should be addressed to M.W. and M.D.